Electronic Supplementary Information

Vacancy-Induced Manganese Vanadates and Their Potential Application to Li-ion Batteries

Martin K. Dufficy, Lan Luo, Peter S. Fedkiw, Paul A Maggard

Section 1. Materials and Instrumentation.

All reagents were used as supplied by the manufacturer without further purification, including: $Mn(NO_3)_2 \cdot nH_2O$ (99.98%, Alfa Aesar), $Co(NO_3)_2 \cdot 6H_2O$ (98.0%, Alfa Aesar), and NH_4VO_3 (99.99%, Aldrich). Deionized water was used as a reagent in each hydrothermal reaction. The inactive electrode materials consisted of Super P Li (Timcal Graphite & Carbon) and carboxymethyl cellulose (Sigma Aldrich). The electrolyte comprised 1 M lithium hexafluorophosphate salt ($LiPF_6$, BASF) dissolved in ethylene carbonate (EC, 99% pure, Sigma Aldrich) and ethyl methyl carbonate (EMC, Ferro Corp.) 1:1 wt% mixture. Electrolyte solvents were dried in molecular sieves (4Å, Sigma Aldrich) to a water content < 10 ppm. A 25-μm thick separator (Celgard) was used to prevent contact between the working electrode and the Li counter/reference electrode (Sigma Aldrich).

High-resolution Powder XRD data were collected on a RIGAKU R-Axis Spider Powder X-ray diffractometer (graphite monochromatized Cu *K*α radiation) at room temperature. Powder X-ray diffraction patterns were scanned with a step size of 0.02° over the 2θ angular range from 4° to 100° and dwell times of 4 s for each step. Thermogravimetric analyses were taken on a TA Instruments TGA Q50 by loading ~5.0 mg onto a platinum pan. The pan was equilibrated and tared at room temperature and heated to 600 °C at a rate of 5 °C/min in air. The post-heated TGA residues were characterized by powder XRD, as described above. Specific surface areas of **I** was measured on a Quantachrome ChemBET Pulsar TPR/TPD. Samples were preheated to 140 °C under flowing N_2 to degas for 3 h, and then cooled with liquid nitrogen and analyzed using a 30% He/N_2 gas mixture. Both pre-cycled and post-cycled electrodes were imaged on an FEI Verios 460L field-emission scanning electron microscope (FESEM). In a glovebox, post-cycled cells were decrimped, and the working electrode was washed with EMC and dried; exposure to air was limited to the FESEM sample loading. Half-cell cycling experiments were performed on an Arbin BT-2000 while cyclic voltammetry (CV) and electrochemical impedance spectroscopy (EIS) experiments were performed on a Bio-Logic VMP3.

Section 2. Experimental Section.

1. Synthetic Procedures. $Mn_{1.5}(H_2O)(NH_4)V_4O_{12}$ (**I**) was synthesized by mixing of 0.0367 g $Mn(NO_3)_2 \cdot nH_2O$, 0.0400 g NH_4VO_3, and ~1mL H_2O in a molar ratio of 1:2:~300 into a polytetrafluoroethylene Teflon pouch (3" × 3") that was then heat sealed in air. The pouch was placed into a 125 mL polytetrafluoroethylene-lined stainless-steel autoclave that was backfilled with ~40 mL deionized water before closing. The reaction vessel was heated to 130°C for 72 h in a convection oven, then subsequently slowly cooled to room temperature at a rate of 6°C/h. The products were washed with deionized water, collected, and dried at 60°C overnight. Small brown needlelike crystals were obtained in a yield of ~70.0% (based on vanadium). **I** was obtained in high phase purity (> 95%) according to powder X-ray diffraction data in **Figure 1**.

2. Crystal Structure. Crystallographic data with specific bond lengths of **I** are listed in **Table S1**, and CCDC No. 1477963 contains additional crystallographic data for this manuscript. This may be obtained free of charge at www.ccdc.cam.ac.uk/conts/retrieving.html.

3. Electrode Fabrication and Characterization. A slurry comprising 70 wt% **I**, 20 wt% carbon black, and 10 wt% binder was cast on Cu foil. Slurries were cast using the doctor-blade method to a desired thickness (25 or 50 μm, corresponding to 1 or 2 mg cm^{-2} of **I**, respectively). The resulting electrode film was dried in a convection oven at 40°C, punched into 1 cm^2 disks, and dried in a vacuum oven at 110°C overnight. The disks were placed as the working electrode *vs* Li metal in 2032 coin-cells. The electrolyte was added via pipette onto the working electrode (~50 μL) and the separator (~50 μL). A spacer and spring were placed on top of Li metal and the coin-cell was hermetically crimped. Half-cells were given a 24 hour rest period at open circuit prior to electrochemical characterization. We defined the capacity of the half-cells such that a 1-C rate corresponds to 1.2 A g^{-1}. All half-cells were cycled between 10 mV and 3 V vs. Li/Li^+. A formation cycle (one cycle at C/24) was applied to all half-cells prior to electrochemical performance assessments. The capacity for **I** electrodes at various rates (as presented in **Figure 3b** of the text) was determined using the 10^{th} cycle in an experiment. Potentiostatic impedance experiments were performance between 100 kHz and 100 mHz using an amplitude of 10 mV. Prior to running EIS, half-cells were (dis)charged using a current density of 10 mA g^{-1} to a specified voltage followed by constant voltage until a current of C/100.

4. Estimating amount [mol] of Li interested on first lithiation.

$$x\frac{mol_{Li}}{mol_{active}} = C\left[\frac{mAh}{g_{active}}\right] \cdot \frac{MW\ [\frac{g_{active}}{mol_{active}}]}{F\left[\frac{mAh}{mol_{Li}}\right]}$$

where: x: mols inserted on initial cycle

C: capacity on initial cycle

MW: molecular weight of **I**

F: Faraday's constant

$$x\frac{mol_{Li}}{mol_{active}} = 1600\left[\frac{mAh}{g_{active}}\right] \cdot \frac{296.15\ [\frac{g_{active}}{mol_{active}}]}{2.6801e4\left[\frac{mAh}{mol_{Li}}\right]}\ ; \quad x \approx 17.7\ \frac{mol_{Li}}{mol_{active}}$$

5. Ex-Situ Electrode Characterization. Half-cells were charged/discharged using a constant current-constant voltage technique; constant currents of 10 mA g^{-1} were applied to **I** electrodes to reach voltages labeled in **Figure 2a** of the text, followed by constant voltage until a current of C/100. The cell was transferred into the glovebox where it was decrimped, washed with EMC, and vacuum dried overnight at room temperature. Still in the glovebox, the electrode material was scraped off the copper foil current colletor, milled in a mortar and pestle, and sealed in a capillary to prevent contact with air. Powder XRD was run on the samples. The electrode material from *ex-situ* PXRD analysis, described above, was heated to 600°C in air at a heat rate of 5°C min^{-1}.

6. Thermogravimetric analysis. Shown in Figure S1, **I** exhibited one weight-loss step for the structural water and the ammonium ion. Using a heating rate of 5°C min^{-1}, we observed removal of water and ammonium ions starting at ~200°C to 320°C. After the removal of water and ammonia, **I** is decomposed into MnV_2O_6 and V_2O_5, as confirmed by PXRD in the Figure S10. The overall reaction is:

$$2Mn_{1.5}(H_2O)(NH_4)V_4O_{12} \rightarrow 3MnV_2O_6 + V_2O_5 + 3H_2O + 2NH_3$$

(exp. 8.57%, calcd. 8.56%).

7. Infrared spectra. The infrared spectrum of **I**, Figure S2, shows broad absorption bands in the 400 to 1200 cm^{-1} range, arising from V-O and Mn-O vibrations. Broad peaks around 3300-3500 cm^{-1} are consistent with the O-H stretching. Notably, two sharp peaks at 1579 cm^{-1} and 1400 cm^{-1} correspond to the bending mode of H_2O and

NH_4^+, respectively, as confirmed with the infrared spectra of H_2O and $NH_3 \cdot H_2O$.[1] Neither the characteristic peaks of H_3O^+ at 1715 cm^{-1} and 2150 cm^{-1}, nor NH_3 molecules at 1205 cm^{-1} were observed.[1] Therefore, **I** contains both coordinating water molecules and NH_4^+ ions.

Section 3. Figures and Tables

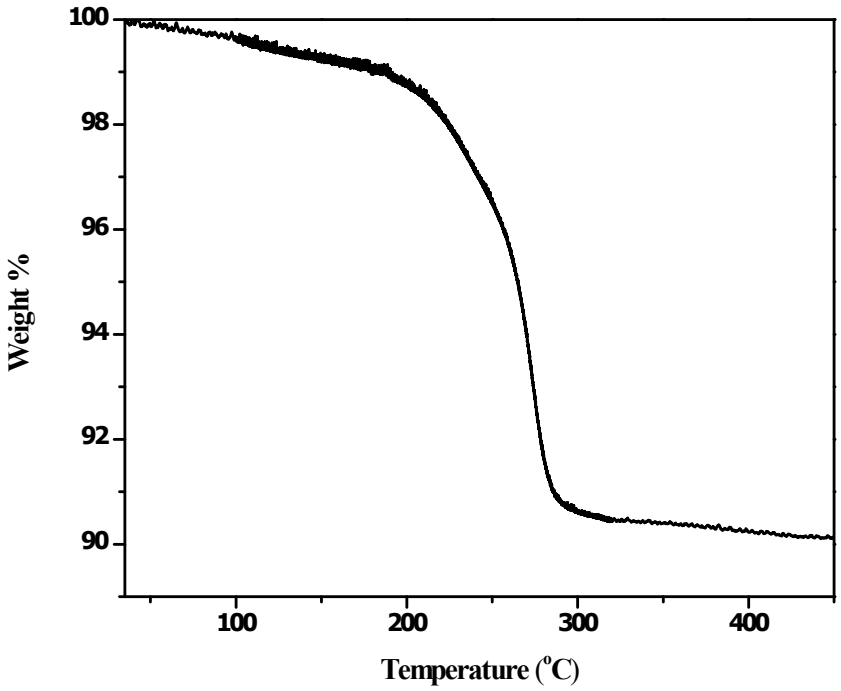

Figure S1. Thermogravimetric analysis for **I** in air plotted as weight (%) versus temperature (°C).

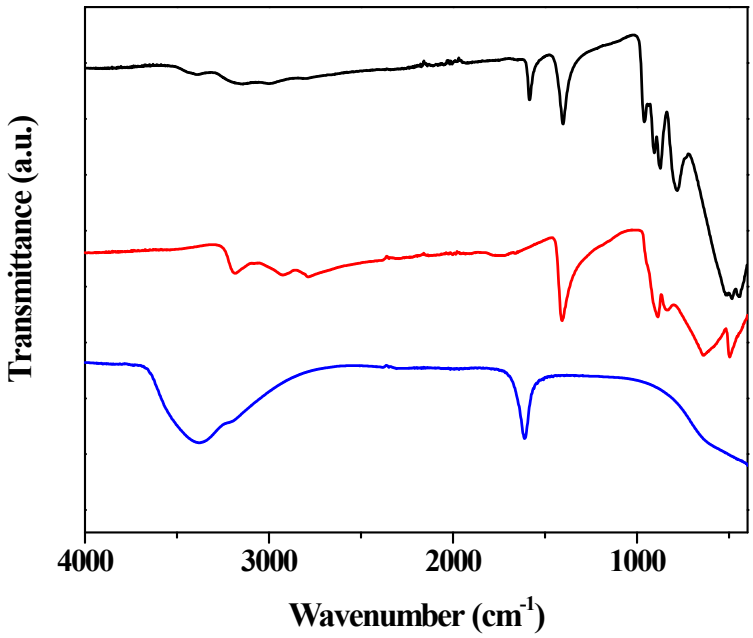

Figure S2. Infrared spectra of **I** (black), H_2O (blue), and NH_3H_2O (red).

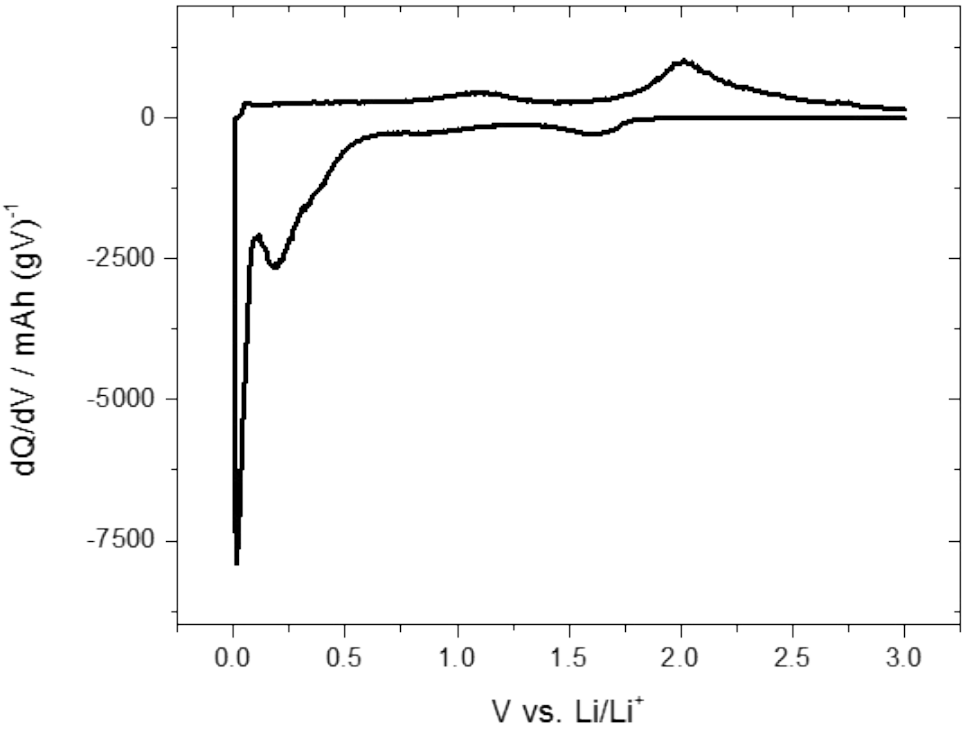

Figure S3. Typical (dis)charge capacity curve derivative profile from constant-current cycling at 10 mA g^{-1}. Peaks denote phase changes that were used for *ex-situ* PXRD studies.

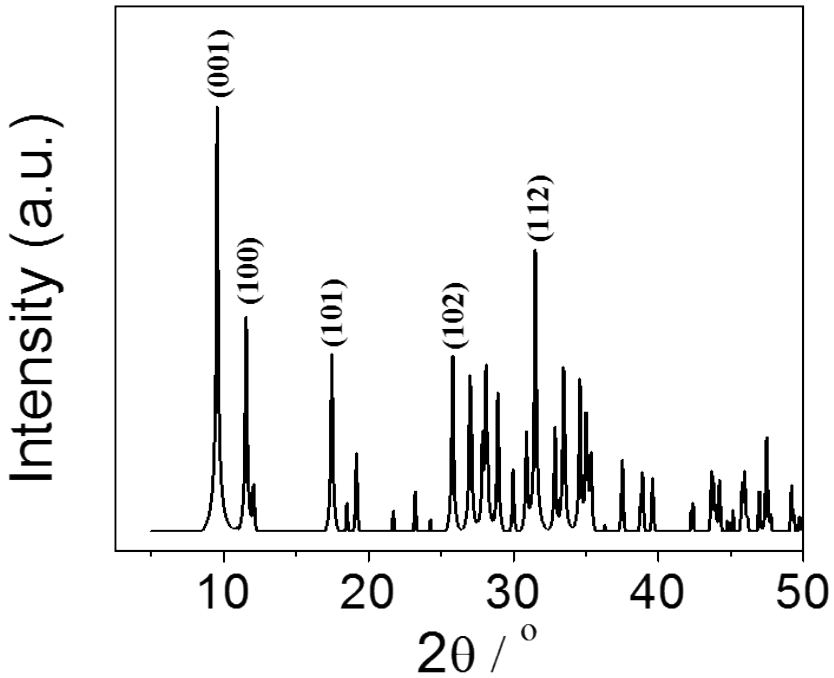

Figure S4. The calculated XRD spectrum of **I**, which agrees with the synthesized structure and proves we created a high-purity, single phase material.

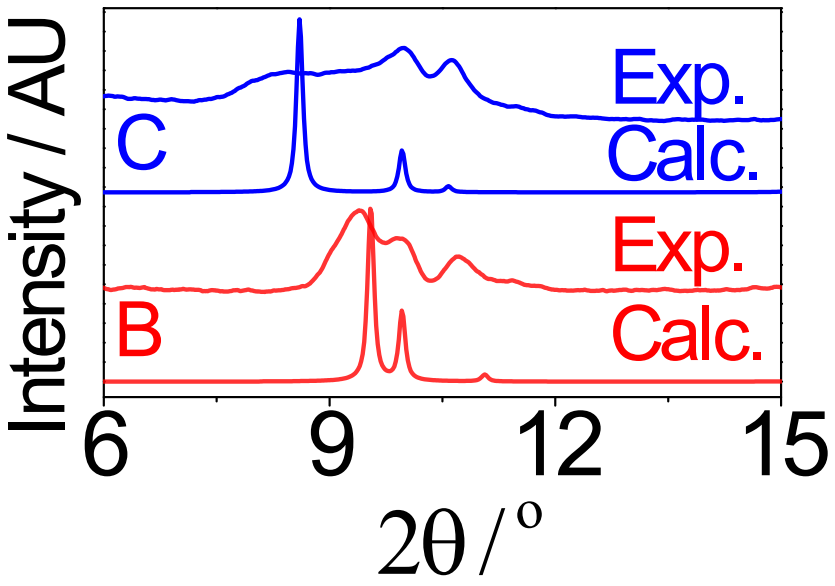

Figure S5. The empirical and simulated low-angle PXRD patterns for **I** electrodes that were lithiated to points **C** and **D**, as described in the text.

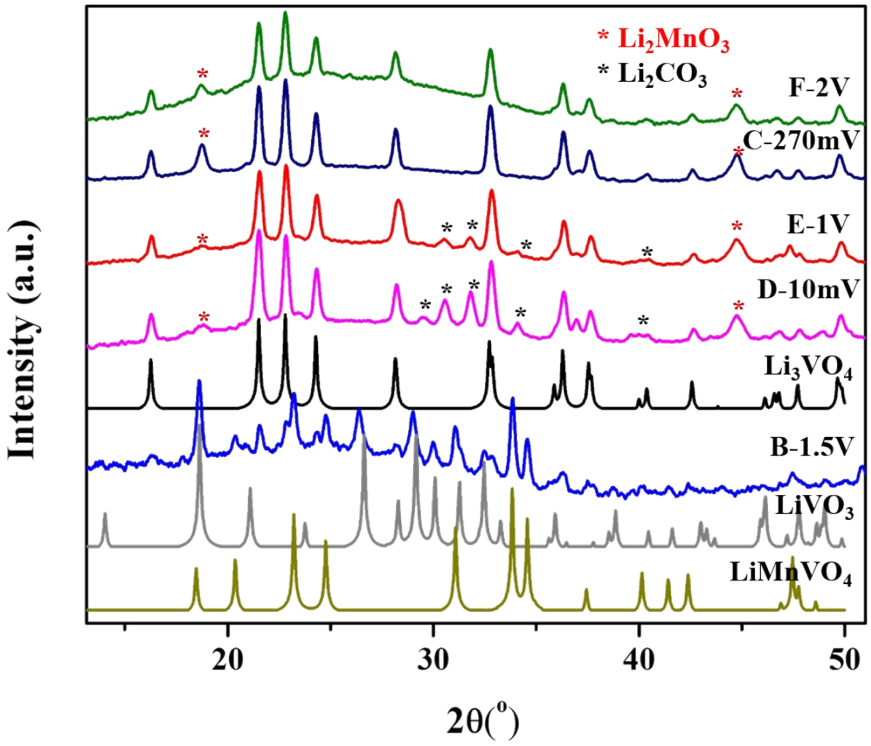

Figure S6. Powder XRD pattern of the thermogravimetric analysis residue for **I** electrodes after charge/discharge cycling and stopped at different voltages, and their assignments. The XRD pattern of **D** revealed a larger presence of Li_2CO_3 (decomposed SEI material) at 10 mV than 270 mV, indicating that SEI formation occurred at low potentials vs. Li/Li+.

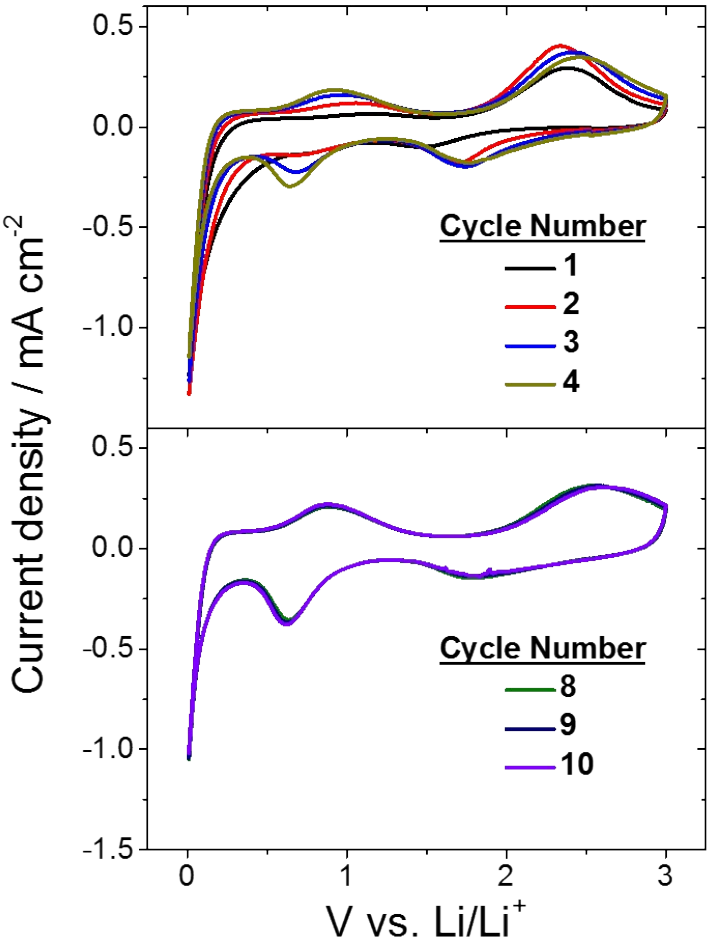

Figure S7. Cyclic voltammetry (CV) on **I** electrodes showing the initial cycling (top) and later cycles (bottom). The first cycle shows single cathodic polarization peak (intercalation) at a potentials near the onset of Li-ion reduction and a single anodic polarization peak (deintercalation) at 2.38 V vs. Li/Li^+. As the cycling progresses, we see a changing voltammogram, as evidence of irreversible reactions and structural rearrangement within **I**; new cathodic peaks arise at ~1.71 and 0.65 V vs. Li/Li^+ and new anodic peaks arise at ~0.93 vs. Li/Li^+. We also see a decrease in cathodic peak current as cycling progresses, which we attribute to Mn dissolution. Peak position becomes constant in later cycles (cycles 8-10) as **I** rearranges into a structure that is stable for (de)intercalation. A scan rate of 0.1 mV s^{-1} was used.

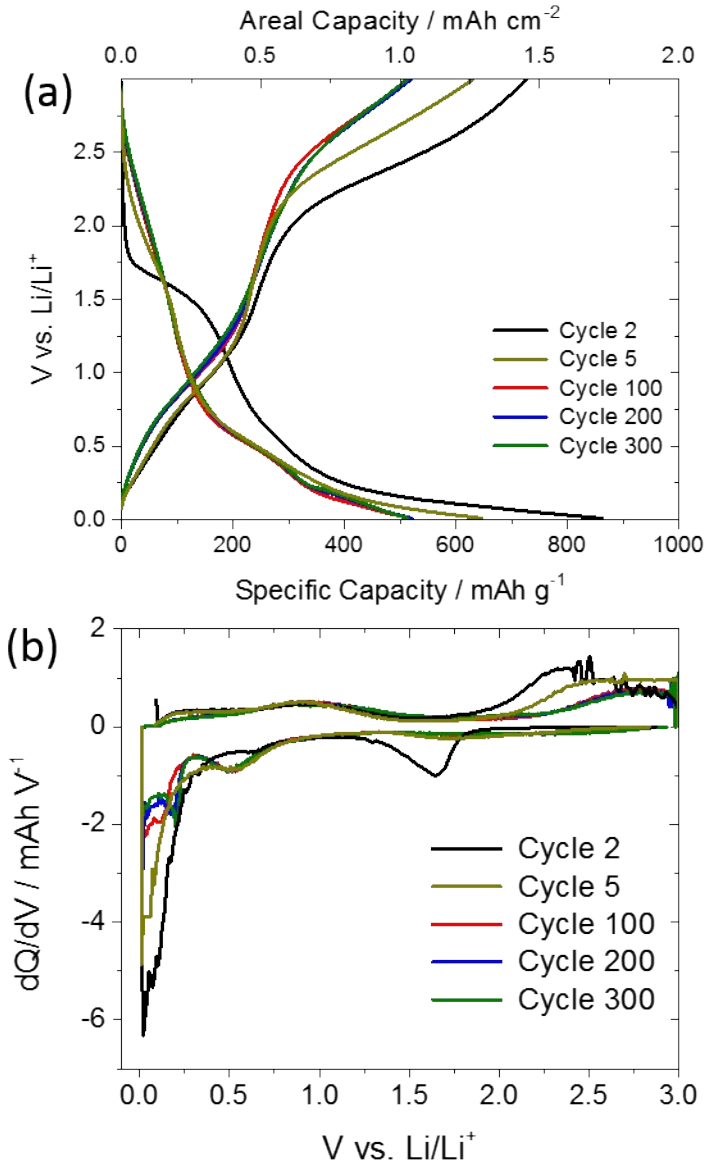

Figure S8. Select half-cell cycling profiles of **I** electrodes, showing (a) the charge/discharge curves and the corresponding (b) derivatives of the charge/discharge curves over 300 cycles. Low-voltage intercalation peaks in (b) decrease in magnitude due to Mn dissolution, however, we observed no significant decrease in low-voltage peak magnitude between cycles 100 and 300.

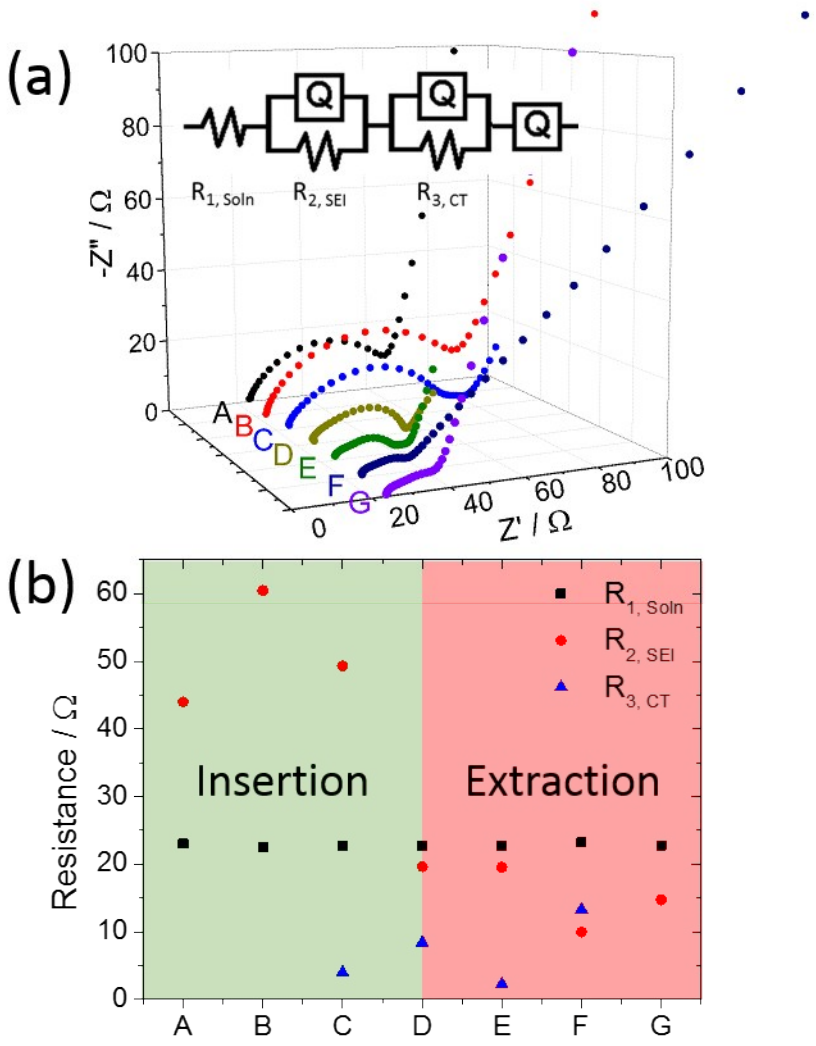

Figure S9. Impedance data for **I** electrodes showing a) Nyquist plots as a function of state-of-charge (SOC) with the equivalent circuit used to fit impedance data; b) values for the resistors when fitting the Nyquist plot to the model equivalent circuit. During the first cycle, the high-frequency resistance values stay constant, which indicates that Mn-ion that may have dissolved in the electrolyte, do not increase the solution resistance. The mid-frequency resistance, corresponding to film resistance from the SEI, decreased in half from points **C** to **D**, or from ~50 Ω at 250 mV to ~19 Ω at 10 mV. The reduction in R2 value with SOC may be associated with decomposition of electrolyte to form a more conductive SEI, as seen in graphite electrodes with similar electrolyte. [2] Upon delithiation, the SEI values do not increase beyond the fully charged state, indicating that a stable SEI has formed. Values of the low-frequency resistance, R3, correspond to the charge transfer resistance. The charge transfer resistance is dependent on mols Li in **I** and diffusivity of Li in **I**. Since the concentration of Li in **I** is high at **D** (near full lithiation after chronoamperometry at 10 mV until C/100, as detailed in the *Experimental Section* above), we see the charge transfer resistance increase due to a lower driving force from the concentration gradient. Charge transfer resistances are large before major Li-insertion at **C** and near full Li-extraction at **G**, and therefore not shown in (b).

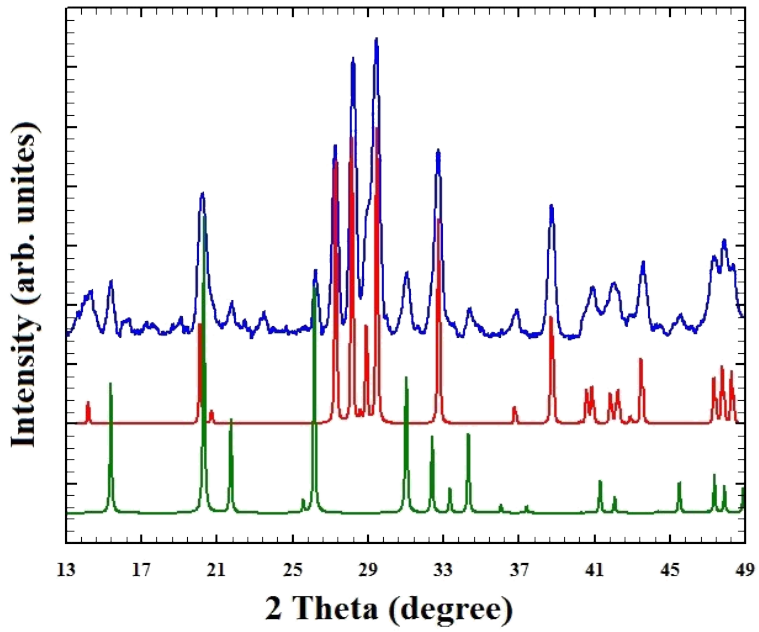

Figure S10. Powder XRD pattern of the TGA residue of **I** after heating in nitrogen (blue), and the calculated MnV_2O_6 pattern (red) and the calculated V_2O_5 pattern (green).

Tables

Table S1. Selected bond distances, angles, and bond valence sums for **I** [a]

Atom1	Atom2	Distance [Å]	Intra-Polyhedral Angle [°]	
Mn1	O6	2.281(1)	O6 – Mn1 – O7	95.54(9)
	O7	2.122(3)	O6 – Mn1 – O7'	84.46(9)
	$\sum S_{ij}$	1.864	O7 – Mn1– O7	180
Mn2	O2	2.235(1)	O5 – Mn2 – O2	88.84(8)
	O5	2.053(2)	O2 – Mn2 – O2'	103.88(9)
	$\sum S_{ij}$	2.184		
V1	O3	2.131(2)	O3 – V1 – O4	73.03(7)
	O4	1.8642(8)	O3 – V1 – O5	151.2(1)
	O5	1.663(2)	O4 – V1 – O6	102.91(9)
	O6	1.652(3)	O4 – V1 – O5	100.52(8)
	$\sum S_{ij}$	5.069	O5 – V1 – O6	103.5(1)
V2	O1	1.613(3)	O1 – V2 – O2	104.6(1)
	O2	1.709(2)	O1 – V2 – O3	105.02(8)
	O3	1.8784(8)	O2 – V2 – O3	99.25(8)
	O4	1.8642(8)	O2 – V2 – O4	152.4(1)
	$\sum S_{ij}$	5.035	O3 – V2 – O4	73.40(7)

[a] $S_{ij} = \exp[(R_0-R_{ij})/B]$, B = 0.37, R_0 = 1.790 Å for Mn^{II} – O, R_0 = 1.803 Å for V^{V} – O.

Table S2: A review of Mn-V anodes in Li-ion half-cells, showing the superior cycling performance of **I** in this study compared to similarly prepared electrodes in literature

Reference in text	Capacity [mAh g^{-1}]	Max Cycle No.	Rate [mA g^{-1}]	Cutoff Voltage
11a [3]	460	50	100	3.4
11b [4]	245	70	0.27-*C* [b]	3.5
11c [5]	450	130	0.25-*C* [b]	3.9
11d [6]	500	50 [a]	100	3.5
13 [7]	500	9 [a]	?	3
This work	500	300	500	3

[a] capacity fading; [b] No basis capacity in text to relate *C*-rate to current

Section 4. References

1) a) E. D. Dzyuba, L. N. Shchegrov and V. V. Pechkovskii, Journal of Applied Spectroscopy 14, 329-332 (1971); b) D. de Waal, A. M. Heyns, K. J. Range and C. Eglmeier, Spectrochimica Acta Part A: Molecular Spectroscopy 46, 1639-1648 (1990); c) J. Hetmańczyk, Ł. Hetmańczyk, A. Migdał-Mikuli and E. Mikuli, Journal of Thermal Analysis and Calorimetry 118, 1049-1056 (2014); d) J. Hetmańczyk, Ł. Hetmańczyk, A. Migdał-Mikuli and E. Mikuli, Spectrochimica Acta Part A: Molecular and Biomolecular Spectroscopy 136, 1515-1522 (2015).
2) S. Zhang, M. S. Ding, K. Xu, J. Allen, T. R. Jow. Electrochemical and Solid-State Letters, 4, 2001, A206-A208.
3) Zhang, S., Hu, R., Liu, L. & Wang, D. Hydrothermal synthesis of MnV2O6 nanobelts and its application in lithium-ion battery. Materials Letters 124, 57-60, (2014).
4) Shuijin, L., Kaibin, T., Yi, J. & Chunhua, C. Preparation of aligned MnV 2 O 6 nanorods and their anodic performance for lithium secondary battery use. Nanotechnology 18, 175605 (2007).
5) Piffard, Y., Leroux, F., Guyomard, D., Mansot, J. L. & Tournoux, M. The amorphous oxides $MnV_2O_{6+\delta}$ ($0 < \delta < 1$) as high capacity negative electrode materials for lithium batteries. Journal of Power Sources 68, 698-703, (1997).
6) Mario Simoes, Y. S., Songhak Yoon, Corsin Battaglia, Simone Pokrant, Anke Weidenkaff. Hydrothermal vanadium manganese oxides: Anode and cathode materials for lithium-ion batteries. Journal of Power Sources 291, 66-74, (2015).
7) Hara, D., Ikuta, H., Uchimoto, Y. & Wakihara, M. Electrochemical properties of manganese vanadium molybdenum oxide as the anode for Li secondary batteries. Journal of Materials Chemistry 12, 2507-2512 (2002).